Role of Tartaric Acid on Structural, Morphological and Optical Properties of FeS_xO_y Films Formed by Chemical Bath Deposition

Abdil Hassan Hidzi[1], Aizuddin Supee[2]*, Nur'ain Balqis Haladin[1], Mohd Zamri Mohd Yusop[1] and Wan Nurulhuda Wan Shamsuri[1]
[1]Universiti Teknologi Malaysia, Johor Bahru, Johor, Malaysia
[2]Energy Management Group, School of Chemical and Energy Engineering, Faculty of Engineering, Universiti Teknologi Malaysia, Johor Bahru, Johor, Malaysia
*Corresponding author (e-mail: aizuddin@utm.my)

Chemical bath deposition (CBD) was used to prepare FeS_xO_y films on fluorine-tin-oxide (FTO)-coated glass substrate. The deposition temperature and time were fixed to 75°C and 3 hours, respectively. In previous works, high concentration of tartaric acid (≥50 mM) led to improvement of the properties of the deposited films [1-2]. However, there is no work reported on CBD of FeS_xO_y with tartaric acid ($C_4H_6O_6$) as the complexing agent. Thus, 50 mM tartaric acid was selected and introduced into the deposition solution containing 100 mM $Na_2S_2O_3$ and 30 mM $FeSO_4$. The pH of the solution with the complexing agent was adjusted close to the pH without the agent (~pH 5.1) using ammonia solution. Both deposited films were crystalline and showed n-type photoresponse. The deposition with tartaric acid resulted in film thickness reduction and contained less iron and larger oxygen and sulfur contents. In addition, the film with 50 mM tartaric acid also showed better homogeneity, improved crystallinity, larger optical transmittance and less hematite peaks. The role of tartaric acid can be explained by considering the suppression of elemental Fe deposition and enhancement of sulfur reduction.

Key words: FeS_xO_y, chemical bath deposition, tartaric acid

Received: October 2019; Accepted: November 2019

Owing to high optical absorption coefficient ($\alpha > 10^5$ cm^{-1} for $\lambda \leq 700$ nm) [3-4] and suitable band gap (Eg = 0.95 eV), FeS_2 could be a potential candidate as an absorber layer in thin film solar cells [5]. In addition, the material extraction cost of FeS_2 only requires 2×10^{-6} ¢/W [6], thus results in the highest rank with regard to the material availability among 23 existing semiconductor material systems that potentially leads to remarkably lower costs than silicon. Its cost effectiveness could be demonstrated as 4% efficiency of FeS_2 cell is equivalent to 20% efficiency of single's crystalline silicon solar [6]. Furthermore, it can exist in n, p and i-type photoresponse [2, 7-10], as well as both direct and indirect transition [11-13], depending on the film composition or impurity (oxygen) inclusion.

Various methods are used to deposit FeS_2 thin films, including chemical bath deposition (CBD) [14-16], electrochemical deposition (ECD) [17-18], spray pyrolysis [12], sulfurization of iron films [19-21], sol-gel deposition [22] and others. Among these, CBD offers the non-vacuum process, economic, capable of large scale deposition and easy control of the deposition parameters.

The role of complexing agents is basically to improve aqueous solution/electrolyte stability, produce sufficient adherence and smooth microstructure. Currently, various complexing agents can be obtained from the market such as tartaric acid ($C_4H_6O_6$), triethanolamine-TEA ($C_6H_{15}NO_3$), ammonia (NH_3), lactic acid ($CH_3CH(OH)COOH$), sodium tartrate ($C_4H_4O_6Na_2$) and ethylenediamine-tetraacetic (acid-EDTA[$CH_2N(CH_2COOH)_2]_2$). In CBD method, Kassim et al. [16] found that the increase in sodium tartrate concentration (0.1-0.3 M) led to reduction of FeS peaks, decreased absorbance and decreased number of grains. Vedavathi et al. [15] discovered that the FeS_2 films deposited with the complexing agents of 0.1 M ethylenediamine-tetraacetic (acid-EDTA) and 10-14 M ammonia were crystalline, and with those 14 M ammonia, pure pyrite phase with better surface morphology and lower film resistivity was obtained. In ECD method, the presence of tartaric acid increased the thickness and reduced oxygen concentration for the deposited FeS_xO_y films [2]. Meanwhile, in successive ionic layer adsorption and reaction (SILAR) method, Manikandan et al. [23] claimed that the triethanolamine presence in the precursor solution resulted in hexagonal shape of the crystalline structure in FeS_2 films.

Nonetheless, there is no such work reported on CBD of FeS_xO_y with tartaric acid as the complexing agent. Thus, the role of tartaric acid on film properties was investigated in this work. Previously, high concentration of tartaric acid (≥50 mM) led to the improvement of the properties of the deposited films [1-2]. Therefore, FeS_xO_y films deposited without the complexing agent were set as the control films, and the effects of 50 mM tartaric acid were studied structurally, morphologically and optically.

EXPERIMENTAL

CBD was performed at 75 °C for 3 hours. Fluorine-tin-oxide (FTO)-coated glass substrate with resistivity of 7 Ω/cm^2 was used to deposit FeS_xO_y films. The deposition area was set to 1 cm × 1 cm by masking on the FTO surface. Prior to each deposition, the substrate was cleaned using alkyl benzene and acetone, and rinsed with deionized (DI) water. A basic aqueous solution containing 100 mM $Na_2S_2O_3$ and 30 mM $FeSO_4$ was used to prepare the control film, and 50 mM tartaric acid as the complexing agent was added to a similar basic solution to prepare the test films. In our previous cyclic voltammetery (CV) measurement [2], larger negative current was obtained when 50 mM tartaric acid was used in the deposition solution. As a result, the properties of the deposited films were improved. Despite a different deposition technique used (electrochemical deposition-ECD), we believe that a similar concentration of tartaric acid would also result in significant effects in our CBD of FeS_xO_y films. The pH of the solution with tartaric acid was adjusted similar to the solution for the control films (about pH 5.1) using ammonia solution, and a magnetic stirrer at 100 RPM was used for both depositions. After CBD process was completed, the films were dried using a dryer and kept in a vacuum box.

Surface morphology, compositional and thickness (via cross-sectional estimation) were analysed using Scanning Electron Microscope (SEM) S-3400N (Hitachi) equipped with Energy Dispersive X-ray (EDX) at a probe voltage of 15 kV. X-ray diffraction (XRD) patterns were recorded by SmartLab X-ray diffractometer (Rigaku) using a CuKα radiation source. The value of 2θ was set in the range of 20-60°. Crystallite size for the films was estimated using a Scherrer equation [24-25]:

$$d = \frac{k\lambda}{\beta \cos \theta} \quad (1)$$

d = average crystallite size- in nm
k = dimensionless shape factor (typical value is about 0.94)
λ = x-ray wavelength (typical value for CuKα is about 0.154056 nm)
β = line broadening at half the maximum intensity (full width at half maximum-FWHM)- in radians
θ = Bragg angle or peak position- in radians

Raman spectra were obtained by LabRAM HR Evolution (HORIBA Scientific) using 633 nm red laser as excitation source. During measurements, the Raman shifts were set from 100-700 cm^{-1} and two different areas were scanned (both areas resulted in similar Raman peaks). Optical transmittance of the films was measured in the range of 350-950 nm using UV-1800 UV-Vis double beam spectrophotometer (Shimadzu Scientific Instruments Inc.). A conventional hot probe method was used to determine the photoresponse, whereby a couple of hot and cold probes were attached to the deposited films. The hot probe was connected to the positive terminal of the multimeter while the cold probe was connected to the negative terminal. For p-type photoresponse, the pointer in the multimeter (under voltage mode) will deflect in negative direction, and vice versa for n-type photoresponse [26-27].

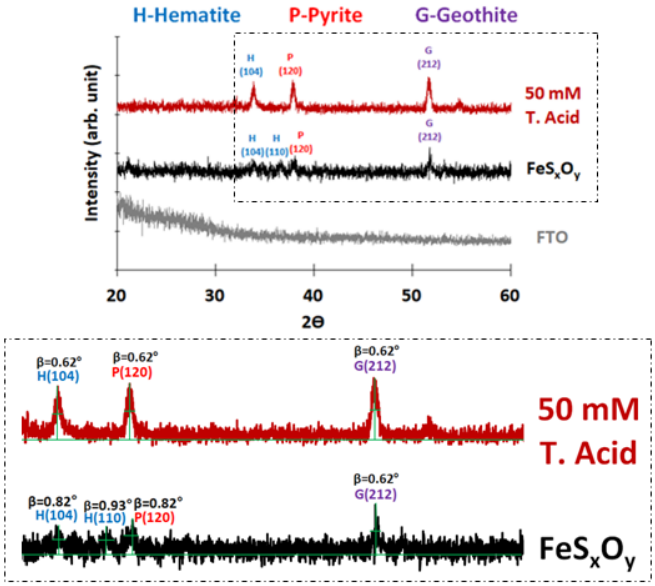

Figure 1. XRD patterns for the measured films.

RESULTS AND DISCUSSION

Figure 1 shows the XRD patterns for the deposited films and FTO substrate. All of the peaks were compared with JCPDS 1309-37-1 (hexagonal hematite-αFe_2O_3), JCPDS 42-1340 (cubic pyrite-FeS_2) and JCPDS 29-0713 (orthorhombic geothite-αFeOOH). There was no peak observed for FTO substrate, while for FeS_xO_y film (0 mM tartaric acid) it yielded an additional hematite peak at $2\theta = 36.36°$. On the other side, the peaks for the film with tartaric acid ($2\theta = 33.81, 36.86, 51.61°$) seemed to be sharper (small peak width of FWHM) than those peaks observed in FeS_xO_y. XRD peak's width can be related to crystallite grain size using a Scherrer equation [24-25]. Average crystallite size is inversely proportional to the peak width of FWHM. Thus, qualitatively small peak width (β), as shown in Figure 1, indicates better crystallinity (larger crystallite grain size). That qualitative statement was verified quantitatively, whereby the average crystallite size for FeS_xO_y and the 50 mM tartaric acid films was estimated in the ranges of 9.4-14.9 nm and 14-14.9 nm, respectively.

Figure 2 illustrates Raman spectra for both the films and FTO substrate. All the peaks are attributed to the deposited films. In previous works, Raman peaks were reported as follows: $Fe_{1-x}S$: 152, 292, 354 cm^{-1} [28]; hematite: 217, 285, 397 cm^{-1} [29-30]; FeS_xO_y: 249, 305 cm^{-1} [31]; and geothite: 298, 397, 414, 474, 550 cm^{-1} [32]. For the measured films, the peaks were as follows: FeS_xO_y (0 mM tartaric acid): 217, 248, 284, 395 cm^{-1}; and 50 mM tartaric acid: 151, 220, 474 cm^{-1}. FeS_xO_y peak only appeared in the control film (0 mM tartaric acid) while for the films with tartaric acid, $Fe_{1-x}S$ and geothite were obtained with less number of hematite peaks.

The thickness of the control film and the films with 50 mM tartaric acid were about 5 µm and 0.4 µm, respectively. Figure 3 depicts the surface morphology for the deposited films. Both the films consisted of inhomogeneous agglomerate formed from various grain size occurring on the surface. Compared to Figure 3(a), the film with 50 mM tartaric acid resulted in larger, dense and uniform agglomeration grains with more well defined boundaries.

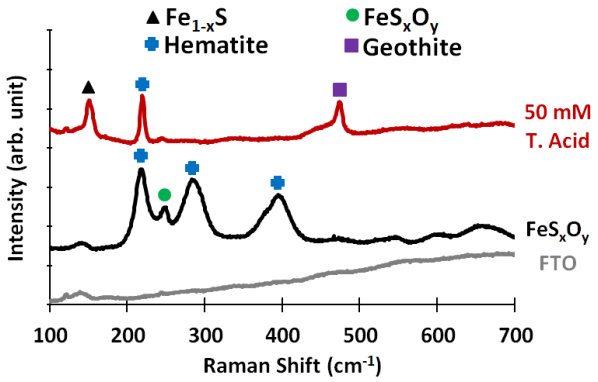

Figure 2. Raman spectra for the measured films and FTO.

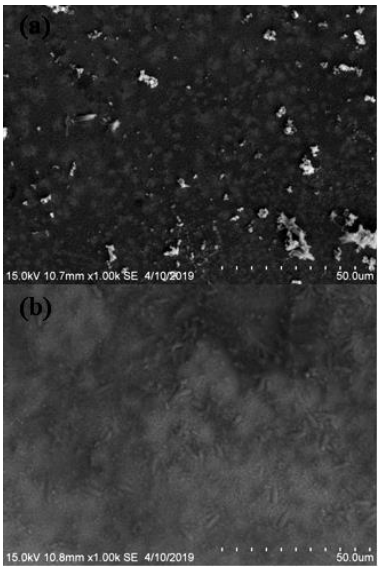

Figure 3. SEM images for the deposited films: (a) FeS_xO_y and (b) 50 mM tartaric acid.

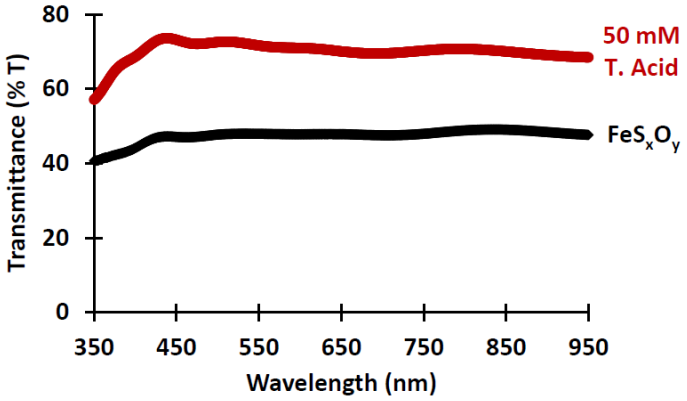

Figure 4. Optical transmittance for the deposited films.

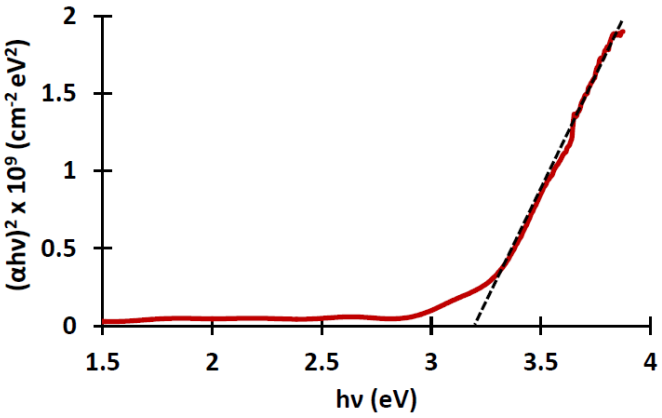

Figure 5. $(\alpha h\nu)^2$ vs. hν for the film deposited with 50 mM tartaric acid.

Table 1. Elemental composition.

Film	Iron-Fe (weight %)	Sulfur-S (weight %)	Oxygen-O (weight %)
FeS_xO_y	51.96	11.18	36.86
50 mM tartaric acid	10.22	32.23	57.55

The optical transmittance for both the films is shown in Figure 4. Higher transmittance is observed for the film with 50 mM tartaric acid. Since the thickness of the film is much smaller than the control FeS_xO_y film, the enhanced transmittance will be mainly due to the reduced thickness.

Clear optical transition slope was found for the film with 50 mM tartaric acid, and thus the direct band gap was estimated by the plot of $(\alpha h\nu)^2$ vs. hν, where α is the absorption coefficient and hν is the photon energy. The plot is shown in Figure 5 and extrapolation of the linear part would intersect x-axis at approximately 3.2 eV.

We further investigated the elemental composition for both the films using EDX and the results are listed in Table 1. The addition of 50 mM tartaric acid into the deposition solution caused in remarkably reduced Fe content and increased S and O contents.

The transformation of pyrite to hematite is a complicated process, and may proceed by different mechanisms under different conditions. Pyrite will be oxidized to form a series of final products, such as hematite (Fe_2O_3), magnetite (Fe_3O_4), geothite (αFeOOH), iron (ferric or ferrous) sulfate ($Fe_2(SO_4)_3$, $FeSO_4$) and sulfur dioxide (SO_2) [33-35]. The transformation process and the formation of these products are influenced by the reaction conditions, such as temperature, oxygen concentration, flow conditions and particle size [33]. Generally, the transformation of pyrite to hematite occurred in the sequence of [33-35]:

$$\text{Pyrite } (FeS_2) \rightarrow \text{Pyrohotite } (Fe_{1-x}S) \rightarrow FeS \rightarrow FeSO \rightarrow FeO \rightarrow \text{Geothite} \rightarrow Fe_2O_3 \quad (2)$$

On the other hand, the use of complexing agents in the deposition solution is common and it is expected that they will form complexes with metal ions and hinder the formation of precipitation (e.g., metal hydroxide) or other spontaneous reactions. In this work, the film deposited with 50 mM tartaric acid resulted in significant iron reduction and higher oxygen and sulfur contents. Oxygen was probably included in the film initially as $Fe(OH)_2$ and then decomposed into iron oxide [2]. With 50 mM tartaric acid, free Fe^{2+}/Fe^{3+} ions concentration in the solution was decreased due to the formation of some complex iron species, and consequently suppressed the formation of $Fe(OH)_2$. Similar phenomena were also observed in previous works [36-37] regarding to the retardation of metal deposition rate for tin (Sn) and iron (Fe) based films. Despite higher oxygen content obtained for the films with 50 mM tartaric acid as shown in Table 1, the complexing agent delayed the transformation of geothite to hematite (Figures 1 and 2), or in other words reduced hematite formation. The transformation of geothite to hematite could be described by the reaction of:

$$Fe(OH)_3 \rightarrow FeO(OH) + H_2O \quad (3)$$

$$2FeO(OH) \rightarrow Fe_2O_3 + H_2O \quad (4)$$

Thus, tartaric acid is considered to suppress the formation of iron oxide. On the other hand, tartaric acid seems to accelerates sulfur reduction in CBD of FeS_xO_y films. This trend was similar with previous works conducted [1-2, 36]. In addition, the film uniformity was enhanced with tartaric acid presence, whereby larger agglomerate size with uniform surface morphology observed in Figure 3(b).

The film deposited with 50 mM tartaric acid showed higher transmittance, sharper XRD peaks and less hematite formation than the control film. According to the Raman spectra in Figure 2, our deposited film with tartaric acid contained $Fe_{1-x}S$, geothite and hematite. Based on the transformation sequence in (2), the transformation of FeS_xO_y to hematite was delayed. Since tartaric acid promotes sulfur reduction and simultaneously suppresses the formation of $Fe(OH)_2$, therefore, the delayed stage was observed with the presence of $Fe_{1-x}S$ and geothite peaks in 50 mM tartaric acid film as depicted in Figure 2. This is probably the reason for the missing peaks as compared to the film without tartaric acid presence. Previously, the band gaps of $Fe_{1-x}S$, geothite ($\alpha FeOOH$) and hematite (αFe_2O_3) were reported to be 0.2 eV [3, 5], 2.5-3.1 eV [38] and 1.87 eV [39], respectively. Based on the plot of $(\alpha h\nu)^2$ vs. $h\nu$ in Figure 5, the direct band gap of the film with tartaric acid is around 3.2 eV. This large band gap value is possibly due to the inclusion of a significant amount of oxygen. Similar findings were also reported regarding to band gap widening of FeS_2 film with oxygen inclusions [40]. This is due to the replacement of sulfur anions with smaller oxygen anions which reduces the average hopping integral within the S ppσ* orbital network. Since the oxygen 2p orbitals are smaller than sulfur 3p orbitals, oxygen anions would act as pinch points in the S ppσ* network and thereby reduce its bandwidth, widening the band gap. Both of the deposited films exhibited n-type photoresponse with high transmission in the visible range, therefore they are suitable as window layers in solar cells application.

CONCLUSIONS

FeS_xO_y thin films have been prepared on FTO-coated glass substrate via CBD at 75°C for 3 hours from an aqueous solution containing $Na_2S_2O_3$ and $FeSO_4$ with controlled pH, and the effects of 50 mM tartaric acid were studied. With the addition of tartaric acid, the film thickness was significantly reduced, sulfur reduction was favoured and hematite formation was reduced. Better film uniformity and crystallinity were obtained for the film with 50 mM tartaric acid. Both films were crystalline and indicated n-type conductivity behaviour. The role of 50 mM tartaric acid in FeS_xO_y film can be explained by considering the retardation of $Fe(OH)_2$ via Fe suppression in which consequently delayed hematite formation.

ACKNOWLEDGEMENTS

The authors gratefully acknowledge the support of the Universiti Teknologi Malaysia and School of Chemical and Energy Engineering for support of this work under Potential Academic Staff (PAS) Grant: Q.J130000.2746.03K25.

REFERENCES

1. Supee, A., Tanaka, Y., Ichimura, M. (2015) Effects of complexing agents on three steps pulse electrodeposited SnS thin films, *Materials Science in Semiconductor Processing*, **38**, 290-297.

2. Supee, A., Ichimura, M. (2016) Effects of complexing agents on electrochemical deposition of FeS_xO_y thin films, *Japanese Journal of Applied Physics*, **55(8)**, 081202.

3. Henríquez, R., Vasquez, C., Briones, N., Munoz, E., Leyton, P., Dalchiele, E. A. (2016) Single phase FeS_2 (pyrite) thin films prepared by combined electrodeposition and hydrothermal low temperature techniques, *International Journal of Electrochemical Science*, **11**, 4966-4978.

4. Qin, H., Jia, J., Lin, L., Ni, H., Wang, M., Meng, L. (2018) Pyrite FeS_2 nanostructures: synthesis, properties and applications, *Materials Science and Engineering: B*, **236-237**, 104-124.

5. Ennaoui, A., Fiechter, S., Pettenkofer, C., Alonso-Vante, N., Büker, K., Bronold, M., Höpfner, C., Tributsch, H. (1993) Iron disulfide for solar energy conversion, *Solar Energy Materials and Solar Cells*, **29(4)**, 289-370.

6. Wadia, C., Alivisatos, A. P., Kammen, D. M. (2009) Materials availability expands the opportunity for large-scale photovoltaics deployment, *Environmental Science and Technology*, **43(6)**, 2072-2077.

7. Walter, J., Zhang, X., Voigt, B., Hool, R., Manno, M., Mork, F., Aydil, E. S., Leighton, C. (2017) Surface conduction in n-type pyrite FeS_2 single crystals, *Physical Review Materials*, **1(6)**, 065403.

8. Srivastava, R., Saxena, A., Ingole, S. (2017) N-type iron pyrite (FeS_2) thin-films obtained at different sulfur vapor pressures, *Chalcogenide Letters*, **14(6)**, 227-237.

9. Supee, A., Ichimura, M. (2017) Three-step pulse electrochemical deposition of FeS_xO_y thin films and their characterization, *Materials Research Express*, **4(3)**, 036410.

10. Bhandari, K. P., Roland, P. J., Koirala, P., Khanal, R. R., Paudel, N. R., Collins, R., Yan, Y., Heben, M. J., Ellingson, R. J. (2015) in *2015 IEEE 42nd Photovoltaic Specialist Conference (PVSC)*, New Orleans, 1-4.

11. Kmentova, H., Kment, S., Hubicka, Z., Remes, Z., Olejnicek, J., Cada, M., Krysa, J., Zboril, R. (2018) Thermal sulfidation of α-Fe_2O_3 hematite to FeS_2 pyrite thin electrodes: correlation between surface morphology and photoelectrochemical functionality, *Catalysis Today*, **313**, 224-230.

12. Orletskii, I., Mar'yanchuk, P., Maistruk, E., Solovan, M., Brus, V. (2016) Low-temperature spray-pyrolysis of FeS_2 films and their electrical and optical properties, *Physics of the Solid State*, **58(1)**, 37-41.

13. Jana, S., Mondal, P., Tripathi, S., Mondal, A., Chakraborty, B. (2015) Electrochemical synthesis of FeS_2 thin film: an effective material for peroxide sensing and terephthalic acid degradation, *Journal of Alloys and Compounds*, **646**, 893-899.

14. Aluri, V., Reddy, K. T. R., Reddy, Y. M. (2015) Polycrystalline and single phase FeS_2 films grown by chemical bath deposition, *Nanotechnology Reviews*, **4(5)**, 469-472.

15. Vedavathi, A., Ramakrishna Reddy, K. T., Munikrishna Reddy, Y. (2015) Role of ammonia on structural, electrical, FTIR and optical studies of FeS_2 films formed by CBD, *International Organization of Scientific Research Journal of Engineering*, **05(02)**, 65-70.

16. Kassim, A., Min, H. S., Yee, L. Y., Tee, T. W., Nagalingam, S. (2012) Complexing agent effect on the properties of iron sulphide thin films, *Canadian Journal of Pure and Applied Sciences*, **6(1)**, 1863-1867.

17. Prabukanthan, P., Thamaraiselvi, S., Harichandran, G. (2017) Single step electrochemical deposition of p-type undoped and Co^{2+} doped FeS_2 thin films and performance in heterojunction solid solar cells, *Journal of the Electrochemical Society*, **164(9)**, D581-D589.

18. Kawai, S., Yamazaki, R., Sobue, S., Okuno, E., Ichimura, M. (2014) Electrochemical deposition of iron sulfide thin films and heterojunction diodes with zinc oxide, *APL Materials*, **2(3)**, 032110.

19. Rajbhandari, P. P., Dhakal, T. P., Westgate, C. R. (2014) in *Photovoltaic Specialist Conference (PVSC), 2014 IEEE 40th*, Denver, 2400-2403.

20. Adusumilli, S. P., Dederick, J. M., Bae, I.-T., Garner, S. M., Sharma, A., Westgate, C. R., Dhakal, T. P. (2016) Iron pyrite thin films grown through a one-step annealing of iron oxide using sulfur sources, tert-butyl disulfide and H_2S, *Thin Solid Films*, **615**, 271-280.

21. Wu, J., Liu, L., Liu, S., Yu, P., Zheng, Z., Shafa, M., Zhou, Z., Li, H., Ji, H., Wang, Z. M. (2014) High responsivity photoconductors based on iron pyrite nanowires using sulfurization of anodized iron oxide nanotubes, *Nano Letters*, **14(10)**, 6002-6009.

22. Kment, S., Kmentova, H., Sarkar, A., Soukup, R. J., Ianno, N. J., Sekora, D., Olejnicek, J., Ksirova, P., Krysa, J., Remes, Z., Hubicka, Z. (2014) Epoxy catalyzed sol–gel method for pinhole-free pyrite FeS_2 thin films, *Journal of Alloys and Compounds*, **607**, 169-176.

23. Manikandan, K., Mani, P., Surendra Dilip, C., Valli, S., Fermi Hilbert Inbaraj, P., Joseph Prince, J. (2014) Effect of complexing agent TEA: the structural, morphological, topographical and optical properties of Fe_xS_x nano thin films deposited by SILAR technique, *Applied Surface Science*, **288**, 76-82.

24. Patterson, A. L. (1939) The Scherrer formula for X-Ray particle size determination, *Physical Review*, **56(10)**, 978-982.

25. Jurkin, T., Štefanić, G., Dražić, G., Gotić, M. (2016) Synthesis route to δ-FeOOH nanodiscs, *Materials Letters*, **173**, 55-59.

26. Axelevitch, A., Golan, G. (2013) Hot-probe method for evaluation of majority charged carriers concentration in semiconductor thin films, *Facta universitatis-series: Electronics and Energetics*, **26(3)**, 187-195.

27. Seeger, K. (2013) *Semiconductor physics: an introduction*, Springer Berlin Heidelberg, London.

28. Bi, Y., Yuan, Y., Exstrom, C. L., Darveau, S. A., Huang, J. (2011) Air stable, photosensitive, phase pure iron pyrite nanocrystal thin films for photovoltaic application, *Nano Letters*, **11(11)**, 4953-4957.

29. Morrish, R., Silverstein, R., Wolden, C. A. (2012) Synthesis of stoichiometric FeS_2 through plasma-assisted sulfurization of Fe_2O_3 nanorods, *Journal of the American Chemical Society*, **134(43)**, 17854-17857.

30. Xiao, W., Wang, Z., Guo, H., Li, X., Wang, J., Huang, S., Gan, L. (2013) Fe_2O_3 particles enwrapped by graphene with excellent cyclability and rate capability as anode materials for lithium ion batteries, *Applied Surface Science*, **266**, 148-154.

31. Umehara, M., Takeda, Y., Azuma, H., Motohiro, T. (2012) Laser annealing to form high-temperature phase of FeS_2, *Japanese Journal of Applied Physics*, **51(2S)**, 02BP10.

32. Thibeau, R. J., Brown, C. W., Heidersbach, R. H. (1978) Raman spectra of possible corrosion products of iron, *Applied Spectroscopy*, **32(6)**, 532-535.

33. Hu, G., Dam-Johansen, K., Wedel, S., Hansen, J. P. (2006) Decomposition and oxidation of pyrite, *Progress in Energy and Combustion Science*, **32(3)**, 295-314.

34. Mitchell, R. E., Mechanisms of pyrite oxidation to non-slagging species, Stanford University (US), 2002.

35. Gialanella, S., Girardi, F., Ischia, G., Lonardelli, I., Mattarelli, M., Montagna, M. (2010) On the goethite to hematite phase transformation, *Journal of Thermal Analysis and Calorimetry*, **102(3)**, 867-873.

36. Brownson, J. R., Georges, C., Larramona, G., Jacob, A., Delatouche, B., Lévy-Clément, C. (2008) Chemistry of tin monosulfide (δ-SnS) electrodeposition effects of pH and temperature with tartaric acid, *Journal of the Electrochemical Society*, **155(1)**, D40-D46.

37. Cheng, S., He, Y., Chen, G. (2008) Structure and properties of SnS films prepared by electro-deposition in presence of EDTA, *Materials Chemistry and Physics*, **110(2–3)**, 449-453.

38. Zhang, H., Bayne, M., Fernando, S., Legg, B., Zhu, M., Penn, R. L., Banfield, J. F. (2011) Size-dependent bandgap of nanogoethite, *The Journal of Physical Chemistry C*, **115(36)**, 17704-17710.

39. Saeed Akhtar, M., Alenad, A., Azad Malik, M. (2015) Synthesis of mackinawite FeS thin films from acidic chemical baths, *Materials Science in Semiconductor Processing*, **32**, 1-5.

40. Hu, J., Zhang, Y., Law, M., Wu, R. (2012) Increasing the band gap of iron pyrite by alloying with oxygen, *Journal of the American Chemical Society*, **134(32)**, 13216-13219.